

## Denoising AMP for MRI Reconstruction: BM3D-AMP-MRI\*

Ender M. Eksioglu<sup>†</sup> and A. Korhan Tanc<sup>‡</sup>

**Abstract.** There is a recurrent idea being promoted in the recent literature on iterative solvers for imaging problems, the idea being the use of an actual denoising step in each iteration. We give a brief review of some algorithms from the literature which utilize this idea, and we broadly label these algorithms as Iterative Denoising Regularization (IDR) algorithms. We extend the Denoising Approximate Message Passing (D-AMP) algorithm from this list to the magnetic resonance imaging (MRI) reconstruction problem. We utilize Block Matching 3D (BM3D) as the denoiser of choice for the introduced MRI reconstruction algorithm. The application of the denoiser for complex-valued data necessitates a special handling of the denoiser. The use of the adaptive and image-dependent BM3D image model prior together with D-AMP results in highly competitive MRI reconstruction performance.

**Key words.** image reconstruction, magnetic resonance, message passing, block matching, compressed sensing, denoising

**AMS subject classifications.** 47A52, 49M30, 65J22, 94A08

**DOI.** 10.1137/18M1169655

### 1. Introduction.

**1.1. A new breed of algorithms on the horizon: Iterative denoising regularization.** Iterative algorithms for the solution of linear inverse problems in imaging can get interpreted as a competition between two forces. These two competing principles acting on the reconstructed image might be summarized as the data fidelity, which enforces adherence to the observation through the forward operator, and the model fidelity, which usually acts through a regularization term to enforce compliance with an image model prior [13]. Iterative thresholding algorithms [7], approximate message passing (AMP) [8], and decoupled approaches [43] for regularized image reconstruction can be seen as different manifestations of the struggle between these two forces. Among these algorithms, AMP introduces the Onsager correction term, which at each iteration approximately Gaussianizes the residual error [27]. The Onsager term enhances the reconstruction performance of AMP when compared to other iterative solvers [8].

The very recent literature on the regularized iterative solutions of imaging problems has seen an idea being independently and repeatedly reintroduced under different disguises. This simple but strong idea is the utilization of actual denoising algorithms for the image model

---

\*Received by the editors February 7, 2018; accepted for publication (in revised form) July 19, 2018; published electronically September 18, 2018.

<http://www.siam.org/journals/siims/11-3/M116965.html>

<sup>†</sup>Electronics and Communication Engineering Department, Istanbul Technical University, Istanbul 34469, Turkey ([eksioglu@itu.edu.tr](mailto:eksioglu@itu.edu.tr)).

<sup>‡</sup>Corresponding author. Department of Biomedical Engineering, Biruni University, Istanbul 34020, Turkey ([atanc@biruni.edu.tr](mailto:atanc@biruni.edu.tr)).

prior of the iterative reconstruction algorithms. Denoising is a well-matured art with estimates to the bound on the optimal performance close to the limits of current algorithms [2]. Denoising algorithms are still getting polished to improved performances with each generation such as the recently introduced global image denoising paradigm [39]. There have been quite a few concurrent and independent algorithms which have incorporated denoising as a distinct substep in iterative image reconstruction. We would like to brand this novel breed of algorithms under the term Iterative Denoising Regularization (IDR). We first want to give a noncomprehensive list of the methods which have utilized this idea independently and in a rather short time span. One of the earliest examples for methods utilizing denoising explicitly as a substep is the iterative decoupled deblurring Block Matching 3D (BM3D) (IDD-BM3D) method of [6]. Here, a game theoretic equilibrium condition is used to decouple the denoising and blur inversion steps. The Plug-and-Play Prior (P&PP) framework of [38] on the other hand uses denoising as a substitute for one of the substeps of the alternating direction method of multipliers (ADMM). The P&PP framework has been applied to bright-field electron tomography in [38], to superresolution and single-photon imaging in [1], and to compressive sampling image recovery in [21]. The model-based image reconstruction (MBIR) model [41] presents a potent framework for the possible inclusion of denoising in iterative image reconstruction. Reference [32] presents an example for the application of iterative denoising regularization to tomographic reconstruction using the MBIR approach. In [32] a quadratic data fidelity term is combined with a model prior term composed of  $\ell$  denoisers with different parameters. Another iterative reconstruction algorithm which has been extended to the IDR setting is the Vector AMP (VAMP) algorithm [34]. VAMP provides a robust AMP variant which has a rigorous state evolution analysis even for the case of ill-conditioned measurement matrices. Reference [4] studies the use of the BM3D denoiser together with VAMP in radar coded-aperture imaging.

The iterative decoupled inpainting BM3D (IDI-BM3D) algorithm of [19] uses BM3D denoising as a substep of a variable splitting based solution for the inpainting problem. The iterative decoupled transform domain inpainting (IDTDI) algorithm of [20] extends the work in [19] and the IDI-BM3D algorithm to inpainting in a transform domain. The Regularization by Denoising (RED) engine from [37] utilizes for regularization a prior term proportional to the inner product between the current image estimate and its denoising residual.

The BM3D-MRI algorithm of [10] utilizes the decoupled image restoration framework as introduced in [43]. BM3D denoising is used as the prior step of this decoupled framework in the magnetic resonance imaging (MRI) reconstruction setting. As additional IDR examples, there have been two concurrent attempts to reconcile AMP with actual denoising algorithms. These attempts include the denoising-based AMP (D-AMP) of [27] and the denoising AMP framework in [40]. In D-AMP [27], a numerical method to approximately calculate the Onsager correction for general denoisers has been developed. D-AMP has already been applied to computed tomography (CT) in [28], to image phase retrieval in [26], and to Compressed Sensing (CS) image recovery in [27] with promising results. In almost all of the above listed IDR examples a common thread has been the usage of the powerful BM3D denoiser [5]. BM3D was used as the only denoiser [4, 6, 10, 19, 20, 28] or as one of the possible denoisers [21, 27, 38, 40] for enforcing the image model prior in an IDR setting.

**1.2. Contributions.** In this work we will introduce a new algorithm for the MRI reconstruction problem based on the D-AMP algorithm [27].<sup>1</sup> We will be using BM3D as the denoiser of choice. The introduced algorithm is designed for possibly complex MR data, which necessitates a special and novel handling of the BM3D denoiser. This novel application of D-AMP in the MRI setting combines the benefits of the adaptive, image-dependent, and nonlocal BM3D image model and the AMP algorithm boosted by the Onsager correction. This combination results in improved performance when compared to state-of-the-art CS-based reconstruction algorithms. The outline for the rest of the paper is as follows. In section 2, we will first introduce the D-AMP-MRI framework. Then we will develop the BM3D-AMP-MRI algorithm, by devising a novel procedure for processing possibly complex data. In this section we give a step-by-step outline of the BM3D-AMP-MRI algorithm. We compare the BM3D-AMP-MRI algorithm to related work from the literature, and we discuss some implementation details. In section 3, we compare the MRI reconstruction performance of the BM3D-AMP-MRI algorithm with recent competing methods from the literature. We also realize different complex domain variants for the BM3D denoising approach. We include both complex and real MR images, three types of sampling masks, and differing sampling ratios. In the conclusions we will review the proposed method.

## 2. MRI reconstruction using BM3D-AMP.

**2.1. Application of D-AMP to MRI reconstruction: D-AMP-MRI.** The observation forward model for MRI is modeled as follows [10]:

$$(1) \quad \mathbf{y} = \mathcal{F}_\Omega \hat{\mathbf{x}} + \boldsymbol{\eta}.$$

$\hat{\mathbf{x}} \in \mathbb{C}^N$  denotes the latent image in a vectorized form. The operator  $\mathcal{F}_\Omega : \mathbb{C}^N \rightarrow \mathbb{C}^M$ , with  $M < N$ , denotes the subsampled Fourier transform, where  $\Omega \in \{1, 2, \dots, N\}^M$  is the set of indices for the partial Fourier data included in  $\mathbf{y}$ . Hence,  $\Omega$  defines the sequence of sample locations included in the MRI acquisition procedure [9].  $\boldsymbol{\eta} \in \mathbb{C}^M$  is additive observation noise. The D-AMP [27] algorithm for MRI reconstruction is formulated as follows:

$$(2a) \quad \mathbf{r}^t = \mathbf{x}^{t-1} + \mathcal{F}_\Omega^H \mathbf{z}^{t-1},$$

$$(2b) \quad \sigma^t = \frac{\|\mathbf{z}^{t-1}\|_2}{\sqrt{N}},$$

$$(2c) \quad \mathbf{x}^t = D_{\sigma^t}(\mathbf{r}^t),$$

$$(2d) \quad \mathbf{o}^t = \mathbf{z}^{t-1} D'_{\sigma^t}(\mathbf{r}^t)/M,$$

$$(2e) \quad \mathbf{z}^t = \mathbf{y} - \mathcal{F}_\Omega \mathbf{x}^t + \mathbf{o}^t.$$

Here,  $\mathcal{F}_\Omega^H : \mathbb{C}^M \rightarrow \mathbb{C}^N$  is the adjoint operator for  $\mathcal{F}_\Omega$  which realizes zero-filled reconstruction.  $\mathbf{x}^t$  is the reconstructed image estimate at the  $t$ th iteration.  $D_\sigma$  is the denoiser operator tuned for a particular noise deviation  $\sigma$ .  $D'_\sigma$  is the divergence of that particular denoiser. The divergence is approximated using a Monte Carlo method, as detailed in [27] and [31], when there is no closed form formulation for the denoiser.  $\mathbf{o}^t$  is the so-called *Onsager correction* term, which

---

<sup>1</sup><http://dsp.rice.edu/software/DAMP-toolbox>

improves the performance of the algorithm by increasing the Gaussianity of the residual term  $\mathbf{z}^t$  [27]. The algorithm is similar to the regular AMP and other iterative shrinkage algorithms. However, the usual frame shrinkage step has been replaced by a denoising step, (2c). We can call (2a) the data fidelity step, where adherence to the observation  $\mathbf{y}$  is emphasized. (2c) can be called the model fidelity step, where the image prior model is enforced via a denoising step.

**2.2. BM3D as the denoiser in D-AMP: BM3D-AMP-MRI.** We will utilize BM3D as the denoiser of choice in this setting. BM3D as introduced in [5] and detailed in [6] calculates an adaptive sparsity model for the specific image under consideration. The BM3D framework originally includes a thresholding step succeeded by a Wiener filtering step. In this work we will only consider the initial thresholding step of the BM3D model, and we will omit the Wiener filtering step. Without the secondary Wiener filtering step, the BM3D denoiser simplifies to a shrinkage operation under an overcomplete frame [6]. In our simulations we have observed that using the full denoising setup with the Wiener filter does not significantly enhance the reconstruction performance despite the increased computational complexity. Under this assumption, the image-dependent sparsity model as introduced by the BM3D is realized by a heuristic shrinkage operation [11] as follows:

$$(3) \quad D_\sigma(\mathbf{x}) = \Psi[\Phi\mathbf{x}]_\lambda.$$

Here,  $\Phi$  is the image-dependent BM3D analysis frame, which is learned for a given image using patch similarities [6].  $\Psi$  is the corresponding synthesis frame, which is calculated as a dual to  $\Phi$  [6]. The  $[\cdot]_\lambda$  operator denotes the thresholding operation applied on the calculated 3D spectral coefficients, where  $\lambda$  denotes the thresholding constant. The thresholding operator is taken to be hard-thresholding as in the original work [5]. The hard-thresholding operation is calculated as follows:

$$(4) \quad [\omega]_\lambda = \omega \circ (|\omega| \geq \lambda).$$

Here, “ $\circ$ ” indicates the elementwise vector multiplication. The thresholding parameter  $\lambda$  is calculated using the noise standard deviation estimate, i.e.,  $\sigma^t$  in (2b). As in [5],  $\lambda$  is calculated with  $\lambda = \lambda_{3D}\sigma$ , where  $\lambda_{3D}$  is an empirically chosen constant. To calculate the Onsager correction, we extend the divergence of the denoiser for the general complex case as follows:

$$(5) \quad D'_\sigma(\mathbf{x}) \approx \frac{1}{\epsilon} \mathbf{b}^H (D_\sigma(\mathbf{x} + \epsilon \mathbf{b}) - D_\sigma(\mathbf{x})).$$

Here,  $\mathbf{b} \sim \mathcal{CN}(0, \mathbf{I})$  is an independent identically distributed (i.i.d.) complex Gaussian distributed random vector with zero mean and unit variance, and  $\epsilon$  is a small constant. We have adopted the value  $\epsilon = \frac{\|\mathbf{x}\|_\infty}{1000}$ , which has also been utilized in [27]. A detailed derivation for our divergence approximation is provided in Appendix A.

In the MRI reconstruction problem the latent image is complex-valued in general. This raises the problem of applying the BM3D algorithm to the real and imaginary channels of the reconstructed image. The straight application of BM3D separately to the two channels does not result in the best performance. The imaginary channel for the complex MR images generally contains less information when compared to the real channel. Hence, learning a

separate frame from the imaginary channel results in performance degradation. We propose to use the same analysis and synthesis frame pair in both channels, and the frame pair is learned from the real-valued channel. We denoise the two channels separately using this single pair of learned frames. The thresholding parameter is also common for both channels. This approach helps us to learn a well sparsifying frame using the patch similarity structure from the real channel of the denoised image. The resulting algorithm will be called BM3D-AMP-MRI. Similar ideas have been used in [14] and [36]. Reference [14] considers photon-counting computed tomography image denoising, where an improved shared patch grouping based on multiple images is proposed. Reference [36] studies multichannel image denoising by utilizing the correlation in the spectral domain of a localized region. An outline of the BM3D-AMP-MRI algorithm is detailed in Algorithm 1. The  $\Re\{\cdot\}$  and  $\Im\{\cdot\}$  operators in Algorithm 1 denote the real and imaginary parts of the argument vector, respectively. When we realize the BM3D-AMP-MRI algorithm, we will utilize the publicly available implementation of the BM3D denoiser. This implementation operates on real-valued data, and it outputs images in the  $[0, 1]$  range. Hence, we introduce an affine transformation  $\mathcal{T}$  at the beginning of the algorithm that maps the initial zero-filled image estimate into the  $[\Delta, 1 - \Delta]$  range where  $\Delta$  is a small positive parameter utilized to prevent clipping.  $\mathcal{T}^{-1}$  is the corresponding inverse transformation. The resulting BM3D-AMP-MRI algorithm is relatively lucid with almost no parameters to tinker with. In general we have kept all the parameters from BM3D at their default values in [5], including the threshold constant  $\lambda_{3D}$ . Hence, we do not optimize any of the parameters depending on input image, sampling mask type, or subsampling ratio.

**2.3. Comparison of BM3D-AMP-MRI with other methods.** As discussed in [27], when we omit the Onsager term  $\sigma^t$  from the D-AMP algorithm as given in (2), the algorithm becomes equivalent to iterative thresholding. The remaining difference is the fact that the thresholding step has been replaced by denoising. The resulting reduced algorithm has been labeled Denoising-Iterative Thresholding (D-IT) in [27]. The D-IT iteration is summarized as follows:

$$(6a) \quad \mathbf{r}^t = \mathbf{x}^{t-1} + \mathcal{F}_\Omega^H (\mathbf{y} - \mathcal{F}_\Omega \mathbf{x}^{t-1}),$$

$$(6b) \quad \mathbf{x}^t = D_{\sigma^t}(\mathbf{r}^t).$$

If we apply the Onsager-free D-IT in the MRI reconstruction setting, the resulting algorithm would naturally be called D-IT-MRI. If the denoiser is BM3D, the algorithm will be called BM3D-IT-MRI.

An iterative denoising based MRI reconstruction algorithm has already been introduced in [10] under the title of BM3D-MRI. BM3D-MRI utilized the decoupled reconstruction algorithm of [43] together with the BM3D image model. The main iteration of the BM3D-MRI reconstruction algorithm is formulated as follows using the current notation [10]:

$$(7a) \quad \mathbf{r}^t = \underset{\mathbf{x}}{\operatorname{argmin}} \|\mathcal{F}_\Omega \mathbf{x} - \mathbf{y}\|_2^2 + \alpha \|\mathbf{x} - \mathbf{x}^{t-1}\|_2^2,$$

$$(7b) \quad \mathbf{x}^t = \underset{\mathbf{x}}{\operatorname{argmin}} \|\mathbf{x} - \mathbf{r}^t\|_2^2 + \gamma^t \|\Phi^t \mathbf{x}\|_0.$$

Equation (7b) is solved by BM3D denoising just as in (6b). Equation (7a) formulates the data consistency in a Tikhonov regularization setting. In [10], (7a) is solved in the Fourier

**Algorithm 1** BM3D-AMP-MRI Algorithm.

---

*Input:* Observation data,  $\mathbf{y} = \mathcal{F}_\Omega \hat{\mathbf{x}} + \boldsymbol{\eta}$ .

- 1: Initialize:  $\mathbf{x}^0 = \mathbf{0}$ ;  $\mathbf{z}^0 = \hat{\mathbf{y}} = \mathcal{F}_\Omega \mathcal{T}\{\mathcal{F}_\Omega^H \mathbf{y}\}$ ;  $\lambda_{3D}$ .
- 2: **for**  $t := 1, 2, \dots, T$  **do** ▷ main iteration starts
- 3:    $\mathbf{r}^t = \mathbf{x}^{t-1} + \mathcal{F}_\Omega^H \mathbf{z}^{t-1}$  ▷ data fidelity step
- 4:   Generate the frames  $\Phi^t$  and  $\Psi^t$  using  $\Re\{\mathbf{r}^t\}$ . ▷ start defining the denoiser functions
- 5:   Define the real-valued BM3D denoiser operator for  $\mathbf{x} \in \mathbb{R}^N$  :  
 $D_\sigma^r(\mathbf{x}) = \Psi^t [\Phi^t \mathbf{x}]_\lambda$ , with  $\lambda = \lambda_{3D} \sigma$
- 6:   Define the complex-valued denoiser operator for  $\mathbf{x} \in \mathbb{C}^N$  :  
 $D_\sigma(\mathbf{x}) = D_\sigma^r(\Re\{\mathbf{x}\}) + j D_\sigma^r(\Im\{\mathbf{x}\})$
- 7:   Define the approximation for the divergence of the complex-valued denoiser:  
 $D'_\sigma(\mathbf{x}) \approx \frac{1}{\epsilon} \mathbf{b}^H (D_\sigma(\mathbf{x} + \epsilon \mathbf{b}) - D_\sigma(\mathbf{x}))$ , where  $\mathbf{b} \sim \mathcal{CN}(0, \mathbf{I})$  is an i.i.d. random vector  
▷ necessary denoiser functions defined
- 8:    $\sigma^t = \frac{\|\mathbf{z}^{t-1}\|_2}{\sqrt{N}}$  ▷ approximate noise std
- 9:    $\mathbf{x}^t = D_{\sigma^t}(\mathbf{r}^t)$  ▷ model fidelity step
- 10:    $\mathbf{o}^t = \mathbf{z}^{t-1} D'_{\sigma^t}(\mathbf{r}^t)/M$  ▷ calculate the Onsager correction
- 11:    $\mathbf{z}^t = \hat{\mathbf{y}} - \mathcal{F}_\Omega \mathbf{x}^t + \mathbf{o}^t$  ▷ calculate the residual
- 12: **end for** ▷ end of main iteration
- 13: Output reconstructed MR image  $\mathbf{x} = \mathcal{T}^{-1}\{\mathbf{z}^T\}$ .

---

domain using the fact that  $\mathcal{F}_\Omega$  is diagonalized by the full Fourier matrix,  $\mathcal{F}$ . This means  $\mathcal{F} \mathcal{F}_\Omega^H \mathcal{F}_\Omega \mathcal{F}^H = \Lambda_\Omega$ .  $\Lambda_\Omega$  is equal to one at the diagonal elements  $k \in \Omega$  and equal to zero everywhere else [10]. It can be proven that the data fidelity step as given in (6a) is equivalent to the optimization problem given in (7a) for  $\alpha = 0$ .

**Proposition 2.1.** Consider the following quadratic regularization problem, where  $\mathcal{F}_\Omega \in \mathbb{C}^{M \times N}$  is a subsampled unitary matrix, with  $M < N$ :

$$(8) \quad \hat{\mathbf{x}} = \underset{\mathbf{x}}{\operatorname{argmin}} \|\mathcal{F}_\Omega \mathbf{x} - \mathbf{y}\|_2^2 + \alpha \|\mathbf{x} - \mathbf{x}_0\|_2^2.$$

The optimal solution is calculated as

$$(9) \quad \hat{\mathbf{x}} = \mathbf{x}_0 + \frac{1}{1 + \alpha} \mathcal{F}_\Omega^H (\mathbf{y} - \mathcal{F}_\Omega \mathbf{x}_0).$$

The proof for Proposition 2.1 is given in Appendix B. The data fidelity step of IT as given in (6a) can be introduced using a variety of incentives [12, 44], including taking a step in the direction of the gradient. However, Proposition 2.1 states that for the special case of  $\mathcal{F}_\Omega$ , (6a) can be motivated by an optimization problem as in (7a). The algorithm definitions given in (6), (7), and Proposition 2.1 together indicate that the BM3D-IT-MRI algorithm of (6) and the BM3D-MRI algorithm of (7) [10] are related. BM3D-IT-MRI as in (6) is a special case of BM3D-MRI in (7) as  $\alpha \rightarrow 0$ .



The BM3D-AMP-MRI algorithm on the other hand includes the additional benefit of the Onsager correction. Hence, we expect improved performance from the BM3D-AMP-MRI algorithm, when compared to the D-IT-MRI and BM3D-MRI pair of algorithms. In [10], where the BM3D-MRI was introduced, the benefit of using the BM3D model prior in an IDR setting was demonstrated. The Patch-based Nonlocal Operator (PANO) algorithm of [30] is another algorithm which inherently utilizes the nonlocal patch-similarity-based image model. PANO also has impressive reconstruction performance [30]. In [10], BM3D-MRI was shown to have better performance than PANO for the special case of real-valued data. With BM3D-AMP-MRI, we have generalized to the general case of complex-valued data with possibly negative values. We have also extended to the AMP setting with the use of the Onsager correction. Hence, BM3D-AMP-MRI is expected to surpass these previous algorithms.

There are numerous other CS types of MRI reconstruction algorithms. The original Sparse-MRI algorithm of [23] has been succeeded by numerous similar approaches. The members of this plethora of algorithms in general either propose improved methods to solve the sparsity regularized MRI reconstruction cost function or proposed enhanced cost functions with better sparsifying transforms. Some notable examples include the shift-invariant discrete wavelet transform-based MR reconstruction (SIDWT) method [30], the Fast Composite Splitting Algorithm (FCSA) [16], the joint constraint patch-based total variation (JCTV) algorithm [22], and the Wavelet Tree Sparsity MRI (WaTMRI) algorithm [3]. The common thread in most of these algorithms is the use of fixed sparsifying transforms, which range from variants of wavelet transforms to other types of x-lets. PANO, BM3D-MRI, and the proposed BM3D-AMP-MRI algorithms on the other hand utilize image-dependent, adaptive transforms with better sparsification capacity, which was demonstrated by the performance of the PANO and BM3D-MRI algorithms in earlier studies. BM3D-AMP-MRI as proposed here implies even better performance by presenting a combination of the powerful image-dependent, nonlocal model from BM3D with the AMP.

**2.4. Implementation of the BM3D-AMP-MRI algorithm.** In [27], it is stated that for D-AMP parameters might get tuned greedily. Hence, it is simply optimal to tune the denoising algorithm that is employed in D-AMP. In our work, just as in [27], we have utilized all the original parameters for the BM3D denoiser as listed in the original realization [5]. We have also utilized the original  $\lambda_{3D}$  parameter value from [5] for all of the simulations with noise-free data. Hence, the introduced BM3D-AMP-MRI algorithm does not necessitate any simulation setting dependent parameter tuning. There is also a need for the choice of the 3D sparsifying transform which defines  $\Phi$  and  $\Psi$ . As in [5], we choose the 3D transformation as separable into 2D and 1D transformations. The 2D transformation is chosen as a biorthogonal wavelet transform, and the 1D transformation is the Haar transform. All of the utilized parameters are preserved for all the different images, different sampling masks, and different sampling ratios.

For the case of i.i.d. sub-Gaussian observation matrices  $\mathbf{A} \in \mathbb{R}^{M \times N}$  with zero mean, the AMP algorithm has a state evolution (SE) with fixed points when  $M, N \rightarrow \infty$  with fixed  $M/N$  [33]. There have been efforts to extend the SE results to wider classes of transforms; however, the behavior of AMP under general random  $\mathbf{A}$  is still an open problem [35]. The Gaussian i.i.d. distribution property of the measurement matrix is a necessary assumption for

the SE analysis of the AMP [8] and DAMP [27] algorithms. However, this property is not a necessary condition for the performance improvement as brought by the AMP algorithm over the regular iterative thresholding. Regular iterative thresholding methods lack the Onsager term derived from the theory of belief propagation in graphical models. The Onsager term in AMP considerably improves the sparsity-undersampling tradeoff when compared to regular iterative thresholding, because the residual gets a better approximation via Taylor expansion [25]. Hence, even without improved Gaussianity of the residual error at each iteration, the DAMP method is expected to benefit from the Onsager correction for improved reconstruction performance.

In works such as [42] and [33], damping and mean-removal procedures have been utilized to ensure convergence of the Generalized AMP (GAMP) algorithm. These studies suggest that transforms with high peak-to-average singular values lead to divergence.  $\mathbf{A}$  chosen from the set of subsampled unitary matrices is studied as a special case in [33]. It is shown that the Gaussian GAMP (GGAMP) variant converges for subsampled unitary matrices with or without damping [33]. This result follows from the fact that the condition number  $\kappa(\mathbf{A}) = 1$  for subsampled unitary matrices. Another recent work, where again subsampled unitary matrices acting as transformation matrices are studied, is the Orthogonal AMP (OAMP) algorithm of [24]. In [24] it is shown that SE predictions for OAMP agree well with the simulations in the case of partial orthogonal matrices. These recent works suggest that subsampled unitary matrices are rather well suited for use in AMP. In our study here, we have utilized the D-AMP algorithm for the particular case of the well-conditioned observation matrix  $\mathcal{F}_\Omega$  which is also a subsampled unitary matrix with condition number  $\kappa(\mathcal{F}_\Omega) = 1$ . We have not encountered any divergence issues throughout the set of implemented simulations.

### 3. Simulation results.

**3.1. Simulation settings.** For comparison with competing methods, we have utilized both complex- and real-valued MR images. Two of the images are T2-weighted complex-valued brain images which have been adopted from the publicly available toolbox of the PANO algorithm in [30].<sup>2</sup> The other two images are real- and positive-valued bust and chest images. We realize the sampling in the Fourier domain using three different subsampling strategies, which are random, radial, and Cartesian sampling [30]. Three subsampling ratios  $M/N$ , namely 15%, 20%, and 30% subsampling, are utilized. Figure 1 showcases sample subsampling masks in the  $k$ -space.

We realize the proposed BM3D-AMP-MRI together with other methods for performance evaluation. The algorithms for comparison include the zero-filling based method and the TV-based Sparse-MRI [23]. The zero-filling reconstruction gets calculated as  $\mathbf{x}_{ZF} = \mathcal{F}_\Omega^H \mathbf{y}$ . Other implemented methods are the shift-invariant discrete wavelet transform based MR reconstruction (SIDWT) [30] and the PANO method [30]. We also realized the BM3D-IT variant, which is realized by cancelling the Onsager correction from the BM3D-AMP-MRI algorithm. Again, the BM3D-IT variant is actually related to the BM3D-MRI algorithm as introduced in [10]. The SNR (signal-to-noise ratio) is calculated as a measure of performance

---

<sup>2</sup><https://sites.google.com/site/xiaoboxmu/publication>



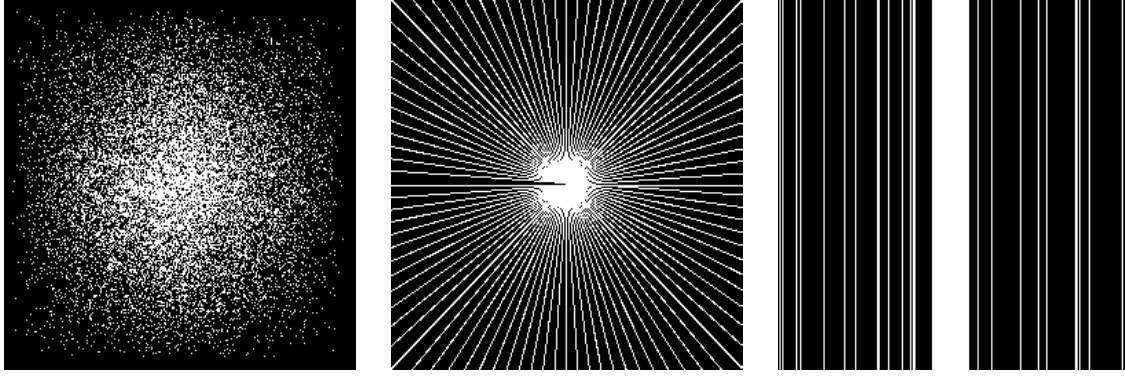


**Figure 1.** Sampling mask examples. Random, radial, and Cartesian sampling masks with 20% subsampling.

for the reconstructed images. SNR in dB is calculated using the images as follows:

$$(10) \quad \text{SNR} = 10 \log_{10} \frac{N}{\|\hat{\mathbf{x}} - \mathbf{x}\|_2^2}.$$

For the BM3D-AMP-MRI and BM3D-IT-MRI realizations, we have made use of the publicly available BM3D toolbox.<sup>3</sup> In particular, we have utilized the color image denoising function to process the real and imaginary valued channels in tandem as previously described in Algorithm 1. The number of outer iterations for the BM3D-based algorithms has been set as  $T = 50$  for real and  $T = 100$  for complex MR images. For the BM3D realization we have assumed the default parameters ( $\lambda_{3D} = 2.7$ ) as defined in the fast implementation of the BM3D toolbox. For complex MR image reconstruction,  $\Delta$  is selected as 0.2. On the other hand, the regularization parameters of SIDWT, PANO, and TV algorithms are optimized as  $10^7$ . In PANO, a single iteration is assumed, and the guide image is reconstructed from the available data. The simulation parameters do not change unless otherwise stated. The simulations were executed in MATLAB using a computer with an Intel i5 CPU at 1.7GHz, 8GB memory, and a 64-bit operating system.

**3.2. Comparison with state-of-the-art algorithms.** In Table 1, we provide the SNR performance of a total of six algorithms for three different masks with 15% subsampling rate. Tables 2 and 3 provide the SNR values with 20% and 30% subsampling rates, respectively. In all tables, we boldface the best SNR result for each particular mask. The BM3D-AMP-MRI has superior performance in most of the different image and mask settings. The PANO algorithm and the BM3D-IT algorithm are generally the next closest contenders in SNR performance. Hence, the algorithms which utilize the nonlocal patch similarity framework have a clear superiority over the more conventional regularization methods. BM3D-IT and PANO have comparable performances, with PANO slightly having the edge. However, the Onsager correction clearly helps, and BM3D-AMP-MRI provides the best overall performance. The performance edge displayed by BM3D-AMP-MRI is more pronounced for 15% and 20% subsampling rates. Table 4 shows the computation time required by the different algorithms for

<sup>3</sup><http://www.cs.tut.fi/~foi/GCF-BM3D>

**Table 1***Reconstruction SNR in dB for different sampling masks under 15% sampling.*

Image Mask	Brain1			Brain2			Bust			Chest		
	Rand.	Radial	Cart.	Rand.	Radial	Cart.	Rand.	Radial	Cart.	Rand.	Radial	Cart.
Zero-filled	22.5	24.6	24.8	21.1	23.7	23.1	18.9	20.8	19.9	17.9	22.2	22.2
TV	29.5	29.7	25.9	28.4	28.3	24.3	27.5	27.1	21.5	23.1	26.3	22.8
SIDWT	31.5	30.7	25.9	30.7	29.5	24.1	27.0	26.9	21.0	23.9	26.2	22.8
PANO	<b>34.6</b>	32.7	26.8	<b>33.7</b>	31.8	25.0	32.9	30.0	22.1	32.0	29.0	23.3
BM3D-IT	32.1	31.5	26.6	29.9	28.0	23.9	33.8	29.8	21.9	30.9	27.5	23.0
BM3D-AMP	33.7	<b>33.4</b>	<b>27.7</b>	<b>33.7</b>	<b>33.5</b>	<b>25.9</b>	<b>34.7</b>	<b>32.7</b>	<b>23.1</b>	<b>34.2</b>	<b>30.4</b>	<b>23.8</b>

**Table 2***Reconstruction SNR in dB for different sampling masks under 20% sampling.*

Image Mask	Brain1			Brain2			Bust			Chest		
	Rand.	Radial	Cart.	Rand.	Radial	Cart.	Rand.	Radial	Cart.	Rand.	Radial	Cart.
Zero-filled	24.9	25.8	25.8	23.9	24.8	24.0	21.0	21.9	21.0	22.0	23.3	23.1
TV	33.4	32.2	27.6	32.3	30.8	26.3	30.8	29.7	24.0	29.2	28.1	24.4
SIDWT	35.3	33.5	27.6	34.1	32.3	26.2	31.2	29.8	22.9	29.8	28.3	24.2
PANO	<b>36.9</b>	35.4	29.5	<b>35.8</b>	34.7	28.2	35.5	32.9	24.9	35.0	31.9	25.4
BM3D-IT	35.5	34.2	28.9	32.6	30.6	25.8	36.5	32.8	24.2	33.7	30.5	24.7
BM3D-AMP	35.9	<b>35.5</b>	<b>30.4</b>	35.5	<b>35.6</b>	<b>28.6</b>	<b>36.6</b>	<b>35.3</b>	<b>25.5</b>	<b>36.5</b>	<b>33.2</b>	<b>25.7</b>

**Table 3***Reconstruction SNR in dB for different sampling masks under 30% sampling.*

Image Mask	Brain1			Brain2			Bust			Chest		
	Rand.	Radial	Cart.	Rand.	Radial	Cart.	Rand.	Radial	Cart.	Rand.	Radial	Cart.
Zero-filled	28.5	27.6	27.8	27.6	26.4	26.2	26.2	23.6	23.1	28.0	24.9	25.2
TV	37.4	36.2	31.2	36.5	34.4	30.4	35.5	33.5	27.5	34.9	31.2	27.6
SIDWT	38.9	38.1	31.1	37.9	36.9	30.5	36.5	34.3	26.4	35.7	30.9	27.1
PANO	<b>40.1</b>	<b>39.6</b>	33.8	<b>39.2</b>	38.6	<b>33.1</b>	39.6	37.6	<b>29.1</b>	39.6	35.8	<b>29.6</b>
BM3D-IT	38.1	37.8	33.0	38.2	35.4	29.4	40.0	37.9	27.7	38.9	35.3	27.8
BM3D-AMP	37.8	37.9	<b>34.5</b>	38.4	<b>38.7</b>	32.9	<b>41.1</b>	<b>39.7</b>	28.7	<b>39.8</b>	<b>36.9</b>	28.9

**Table 4***Computational time requirements for the algorithms.*

Algorithm	BM3D-AMP-MRI	BM3D-IT-MRI	PANO	SIDWT	TV
Time (sec)	120.2	63.6	204.0	123.1	14.3

the sample case of brain images and 20% radial downsampling. BM3D-AMP-MRI requires two denoising operations due to the calculation of the approximate divergence as given in (5). The BM3D denoiser dominates the computational complexity; hence BM3D-AMP-MRI takes approximately twice as long as BM3D-IT. However, the time requirement of BM3D-AMP-MRI is still lower than PANO.

Figures 2 through 5 depict the reconstructed images for a subset of simulations. In these figures, the first row contains the original image (left), TV result (middle), and SIDWT result

Table 5

Reconstruction SNR in dB for different sampling masks under 20% sampling and observation noise with  $-20$  dB power relative to the image power.

Image	Brain1			Brain2			Bust			Chest		
Mask	Rand.	Radial	Cart.	Rand.	Radial	Cart.	Rand.	Radial	Cart.	Rand.	Radial	Cart.
Zero-filled	24.7	25.5	25.5	23.7	24.5	23.7	20.8	21.6	20.8	21.5	22.6	22.5
TV	28.9	28.5	26.3	28.0	27.5	24.9	26.5	25.9	22.4	24.5	24.2	22.6
SIDWT	31.1	30.3	26.7	30.2	29.3	25.3	27.7	26.9	22.2	26.3	25.5	23.1
PANO	32.0	31.3	28.0	31.2	30.5	26.7	29.4	28.3	23.8	28.0	27.0	23.8
BM3D-IT	30.7	29.5	27.6	29.2	28.3	25.4	30.1	29.5	24.6	28.3	28.5	25.0
BM3D-AMP	<b>32.7</b>	<b>32.4</b>	<b>29.4</b>	<b>31.7</b>	<b>31.5</b>	<b>28.3</b>	<b>31.3</b>	<b>30.5</b>	<b>25.8</b>	<b>30.9</b>	<b>29.8</b>	<b>25.6</b>

(right). The second row contains the PANO (left), BM3D-IT (middle), and BM3D-AMP-MRI (right) results. From the SNR results and reconstructed images we can state that the BM3D-AMP-MRI algorithm has superior reconstruction performance with acceptable computational time requirements.

We have also performed experiments in the presence of Fourier domain additive white Gaussian complex noise with a total noise power of  $-20$  dB relative to the image power. The SNR results of the algorithms are provided in Table 5, where the algorithm parameters have been kept the same as in the noiseless case. This table suggests that the BM3D-AMP-MRI algorithm is advantageous when the Fourier domain observation is disturbed by additive noise. We have also conducted experiments for brain MR images with higher levels of noise power. We have optimized the regularization parameter of the PANO algorithm as  $10^2$  and the thresholding parameter of BM3D-AMP-MRI as  $\lambda_{3D} = 4$ . The SNR results are provided in Figure 6. We deduce that the BM3D-AMP-MRI algorithm performs the best in all of the simulation settings realized for the noisy case. The BM3D-AMP-MRI algorithm is more robust to the existence of measurement noise due to inherent usage of a denoiser as a substep.

**3.3. Further simulations.** We have also realized experiments with other forms of complex domain BM3D-type denoising algorithms used in the BM3D-IT-MRI setting. The first of these denoisers is based on the higher-order singular value decomposition (HOSVD) based Complex Domain BM3D (CD-BM3D) denoising algorithm, the details of which are provided in [17, 18]. The second such denoiser is straight application of BM3D to the two channels of the complex MR image, which we denote as independent channel BM3D denoising. In the implementation of the HOSVD based BM3D-IT, we have skipped the Wiener filtering step for computational complexity issues, and we found the optimal threshold parameter as 4. The SNR convergence curves for complex and real MR images are shown in Figures 7 and 8, respectively. For complex MR images, the SNR performance of HOSVD based BM3D-IT falls between that of BM3D-AMP and BM3D-IT algorithms, and IC based BM3D-IT has the worst SNR performance. We measure the runtimes for HOSVD based BM3D-IT and IC based BM3D-IT as  $172.5 \times 10^2$  and 130.9 seconds, respectively. It can be deduced that our BM3D-IT has a definite runtime advantage over the HOSVD based BM3D-IT at a price of slight SNR degradation. Also, comparisons with IC based BM3D-IT confirm the SNR and runtime

**Table 6**  
*KL divergence values for the algorithms.*

Algorithm	Brain1 MR	Brain2 MR	Bust	Chest
BM3D-IT-MRI	0.048	0.039	0.056	0.138
BM3D-AMP-MRI	<b>0.040</b>	<b>0.021</b>	<b>0.020</b>	<b>0.005</b>

advantages of our denoising strategy based on synthesis and analysis frames learned from the real channel. Both figures illustrate the SNR advantage attained by utilizing the Onsager correction. The computational time requirement of the HOSVD based BM3D denoising is very high when compared to the competing denoising methods. Reconstruction using HOSVD based BM3D runs almost 300 times slower when compared to our tandem denoising approach. The simulation results indicate that the tandem denoising procedure as introduced by the manuscript presents a good compromise between reconstruction performance and computation time. Despite having very good denoising performance for complex-valued data, the HOSVD based BM3D denoiser is not the best fit for iterative reconstruction algorithms due to the highly increased complexity.

We also calculated the Kullback–Leibler (KL) divergence of the power spectrum for  $\mathbf{z}^t$  from the white power spectrum as a measure of correlatedness of the residual  $\mathbf{z}^t$ . Strong dependence on the residual leads to a worsening of the prediction of the moments of  $\mathbf{z}^t$  [25]. Hence, an improvement in uncorrelatedness of the residual is expected to lead to performance improvement. We calculate the KL divergence as follows using the definition from [15]:

$$(11) \quad D = \frac{1}{4\pi} \int_{-\pi}^{\pi} \left\{ \frac{P_z(e^{j\omega})}{\sigma_z^2} - \ln \frac{P_z(e^{j\omega})}{\sigma_z^2} - 1 \right\} d\omega = -\frac{1}{4\pi} \int_{-\pi}^{\pi} \ln P_z(e^{j\omega}) d\omega + \frac{\ln \sigma_z^2}{2}.$$

Here  $P_z(e^{j\omega})$  denotes the power spectrum of  $\mathbf{z}^t$ , and  $\sigma_z^2$  denotes the variance of  $\mathbf{z}^t$ , i.e., the constant value of the white power spectrum. We approximate  $P_z(e^{j\omega})$  by using Burg's method [29] with FFT size 1024 and model order 5. We have considered brain, bust, and chest MR images with a radial mask of 20% sampling. The resulting KL divergence values are given in Table 6. We should notice that bigger KL divergence corresponds to higher correlation amongst the samples of  $\mathbf{z}^t$ . We observe that for all cases, BM3D-AMP-MRI produces  $\mathbf{z}^t$  samples with less correlation when compared with those produced by BM3D-IT-MRI.

**4. Conclusions.** Iterative image reconstruction algorithms are in general as good as the utilized image model prior. Denoising algorithms, on the other hand, represent the state-of-the-art in image modeling. Hence, it comes as no surprise that there have been quite a number of recent and independently proposed iterative reconstruction algorithms which incorporate actual denoising as a distinct step for model fidelity. We first identified some of these concurrent novel attempts. D-AMP is one of the important examples from these algorithms. We have utilized the D-AMP framework together with the BM3D denoiser in the MRI reconstruction setting. The use of BM3D necessitates an original handling of the BM3D denoiser, and we name the resulting algorithm BM3D-AMP-MRI. We also show that the case of D-IT which lacks the Onsager correction is equivalent to an algorithm from the literature. BM3D-AMP-MRI merges the power of AMP and Onsager correction with the potential of the

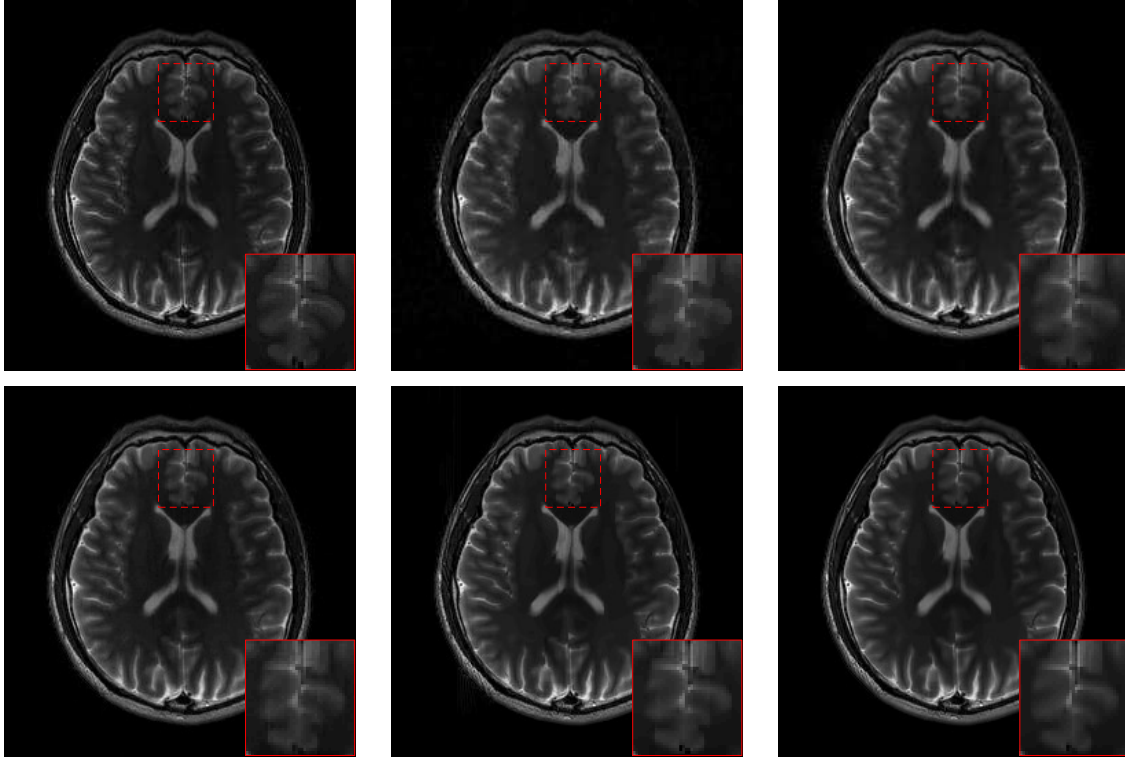


**Figure 2.** Magnitude of the first complex brain image under 20% radial sampling. First row: Original (left), TV (middle), SIDWT (right). Second row: PANO (left), BM3D-IT (middle), BM3D-DAMP (right).

image-dependent, nonlocal, BM3D image model. The algorithm does not need any fine-tuning for any parameter. We apply the BM3D-AMP-MRI algorithm for different MR images and a variety of sampling masks and sampling ratios. BM3D-AMP-MRI provides very competitive reconstruction performance on par with the state-of-the-art algorithms from the literature.

**Appendix A. Divergence for the complex-valued denoiser.** Let us consider a vector-valued function  $\mathbf{f} : \mathbb{C}^N \rightarrow \mathbb{C}^N$  and the vectors  $\mathbf{y}, \mathbf{b} \in \mathbb{C}^N$ . The following is written using Taylor series expansion:

$$(12) \quad \mathbf{f}(\mathbf{y} + \epsilon \mathbf{b}) - \mathbf{f}(\mathbf{y}) = \epsilon \mathbf{J}(\mathbf{y}) \mathbf{b} + \mathcal{O}(\epsilon^2).$$

Here  $\mathbf{J}$  denotes the Jacobian of the argument vector. By multiplying both sides by  $\epsilon^{-1} \mathbf{b}^H$ , we obtain

$$(13) \quad \mathbf{b}^H \frac{\mathbf{f}(\mathbf{y} + \epsilon \mathbf{b}) - \mathbf{f}(\mathbf{y})}{\epsilon} = \mathbf{b}^H \mathbf{J}(\mathbf{y}) \mathbf{b} + \mathcal{O}(\epsilon),$$

where  $\mathbf{b}^H$  is absorbed in  $\mathcal{O}(\epsilon)$  and  $\mathbf{b}^H \mathbf{J}(\mathbf{y}) \mathbf{b}$  is a complex scalar number. We utilize the cyclic property of trace to obtain  $\mathbf{b}^H \mathbf{J}(\mathbf{y}) \mathbf{b} = \text{tr}(\mathbf{b}^H \mathbf{J}(\mathbf{y}) \mathbf{b}) = \text{tr}(\mathbf{J}(\mathbf{y}) \mathbf{b} \mathbf{b}^H)$ . Since  $\mathbf{J}(\mathbf{y})$  is independent of  $\mathbf{b}$  which is complex Gaussian with zero mean and unit variance, we have the

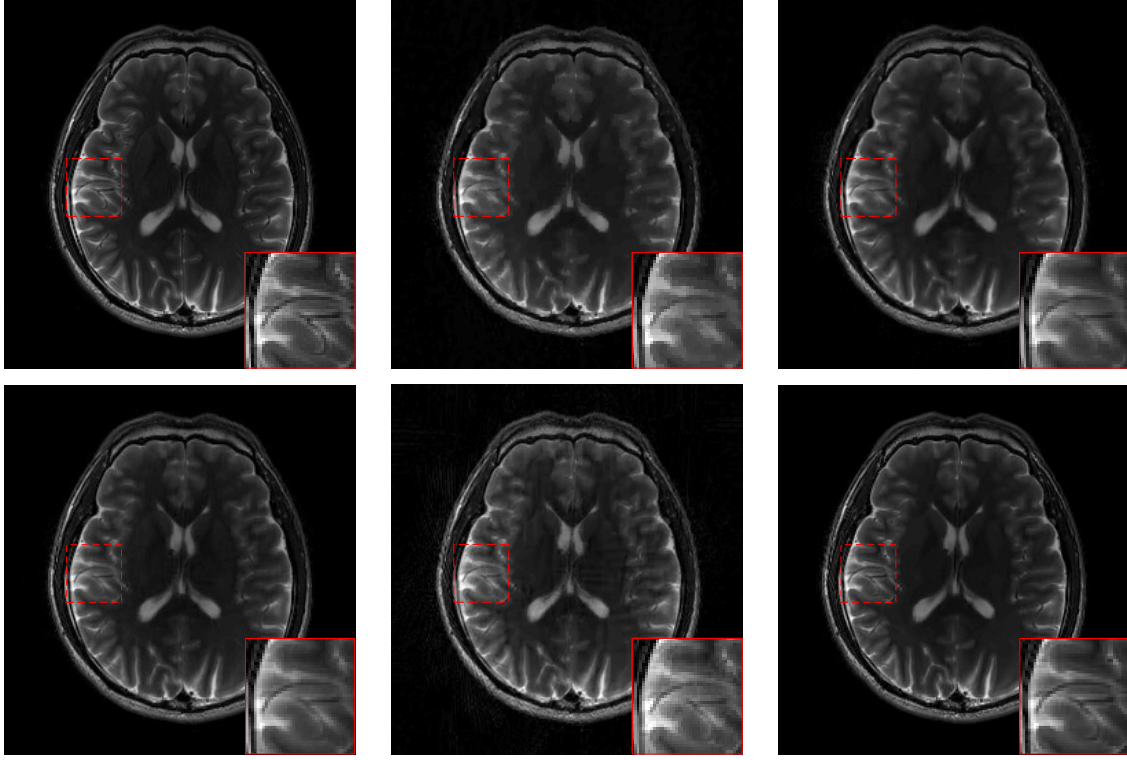


**Figure 3.** Magnitude of the second complex brain image under 20% radial sampling. First row: Original (left), TV (middle), SIDWT (right). Second row: PANO (left), BM3D-IT (middle), BM3D-DAMP (right).

following expectation with respect to  $\mathbf{b}$ :

$$(14a) \quad E\left(\mathbf{b}^H \frac{\mathbf{f}(\mathbf{y} + \epsilon \mathbf{b}) - \mathbf{f}(\mathbf{y})}{\epsilon}\right) = E\left(\text{tr}(\mathbf{J}(\mathbf{y}) \mathbf{b} \mathbf{b}^H)\right)$$

$$(14b) \quad = \text{tr}\left(\mathbf{J}(\mathbf{y}) E(\mathbf{b} \mathbf{b}^H)\right)$$

$$(14c) \quad = \text{tr}(\mathbf{J}(\mathbf{y})).$$

By definition,  $\text{div}\{\mathbf{f}(\mathbf{y})\} = \text{tr}(\mathbf{J}(\mathbf{y}))$  [31] and (5) serves as the deterministic approximation  $\text{div}\{\mathbf{f}(\mathbf{y})\}$ .

**Appendix B. Proof of Proposition 2.1.** We want to calculate the solution to the following optimization problem for the special case of a subsampled unitary matrix  $\mathcal{F}_\Omega \in \mathbb{C}^{M \times N}$ , with  $M < N$ .

$$(15) \quad \hat{\mathbf{x}} = \underset{\mathbf{x}}{\text{argmin}} \|\mathcal{F}_\Omega \mathbf{x} - \mathbf{y}\|_2^2 + \alpha \|\mathbf{x} - \mathbf{x}_0\|_2^2.$$

When we calculate the gradient of the cost function and set it equal to zero we get the following solution:

$$(16) \quad \hat{\mathbf{x}} = (\mathcal{F}_\Omega^H \mathcal{F}_\Omega + \alpha \mathbf{I}_N)^{-1} (\mathcal{F}_\Omega^H \mathbf{y} + \alpha \mathbf{x}_0).$$



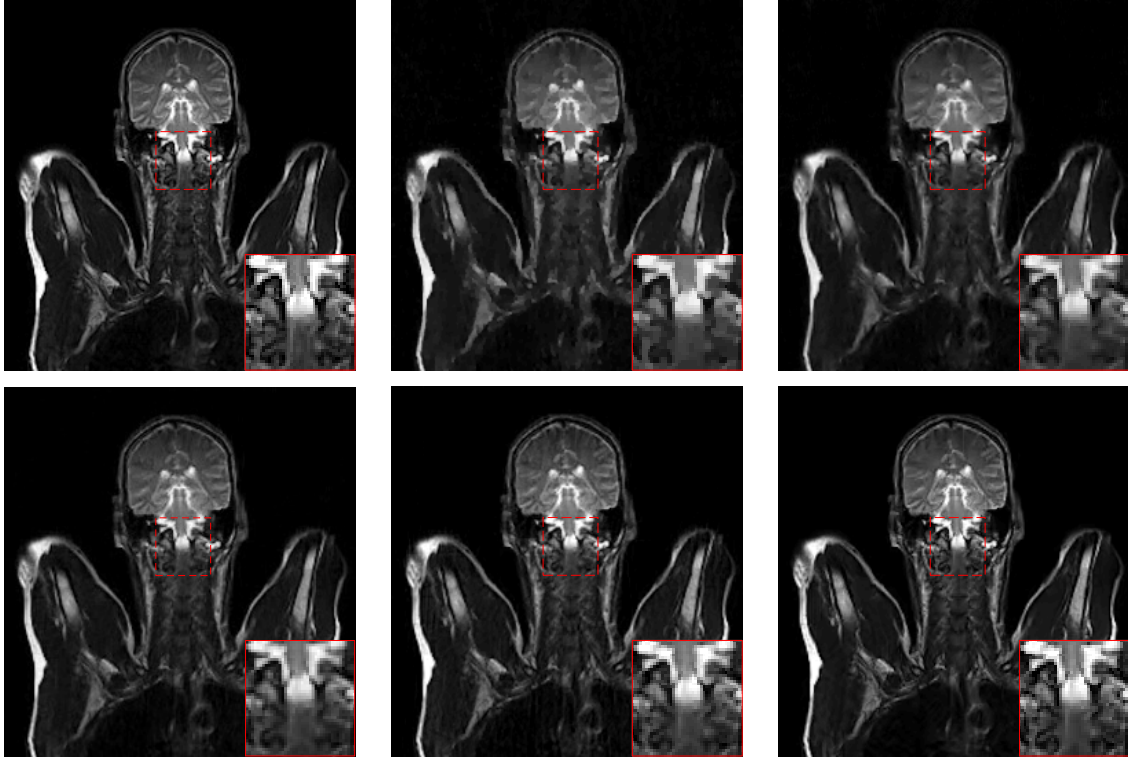


**Figure 4.** Magnitude of the real-valued bust image under 20% radial sampling. First row: Original (left), TV (middle), SIDWT (right). Second row: PANO (left), BM3D-IT (middle), BM3D-DAMP (right).

This solution can equivalently be written as follows:

$$(17) \quad \hat{x} = x_0 + (\mathcal{F}_\Omega^H \mathcal{F}_\Omega + \alpha \mathbf{I}_N)^{-1} \mathcal{F}_\Omega^H (y - \mathcal{F}_\Omega x_0).$$

Now, we will take the Fourier transform of both sides in (17). We will also use the equalities  $\mathcal{F}\mathcal{F}^H = \mathcal{F}^H\mathcal{F} = \mathbf{I}_N$  and  $\mathcal{F}_\Omega\mathcal{F}_\Omega^H = \mathbf{I}_M$ . We note that  $y - \mathcal{F}_\Omega x_0 = \mathcal{F}_\Omega\mathcal{F}_\Omega^H y - \mathcal{F}_\Omega x_0 = \mathcal{F}_\Omega(\mathcal{F}_\Omega^H y - x_0) = \mathcal{F}_\Omega(x_{ZF} - x_0)$ , with  $x_{ZF} = \mathcal{F}_\Omega^H y$ .

$$(18) \quad \mathcal{F}\hat{x} = \mathcal{F}x_0 + \mathcal{F}(\mathcal{F}_\Omega^H \mathcal{F}_\Omega + \alpha \mathbf{I}_N)^{-1} (\mathcal{F}^H \mathcal{F}) \mathcal{F}_\Omega^H \mathcal{F}_\Omega (\mathcal{F}^H \mathcal{F}) (x_{ZF} - x_0).$$

From (18), we can arrive at the following result:

$$(19a) \quad \mathcal{F}\hat{x} = \mathcal{F}x_0 + (\mathcal{F}(\mathcal{F}_\Omega^H \mathcal{F}_\Omega + \alpha \mathbf{I}_N)^{-1} \mathcal{F}^H) (\mathcal{F}\mathcal{F}_\Omega^H \mathcal{F}_\Omega \mathcal{F}^H) \mathcal{F}(x_{ZF} - x_0)$$

$$(19b) \quad = \mathcal{F}x_0 + (\mathcal{F}(\mathcal{F}_\Omega^H \mathcal{F}_\Omega + \alpha \mathbf{I}_N) \mathcal{F}^H)^{-1} (\mathcal{F}\mathcal{F}_\Omega^H \mathcal{F}_\Omega \mathcal{F}^H) \mathcal{F}(x_{ZF} - x_0).$$

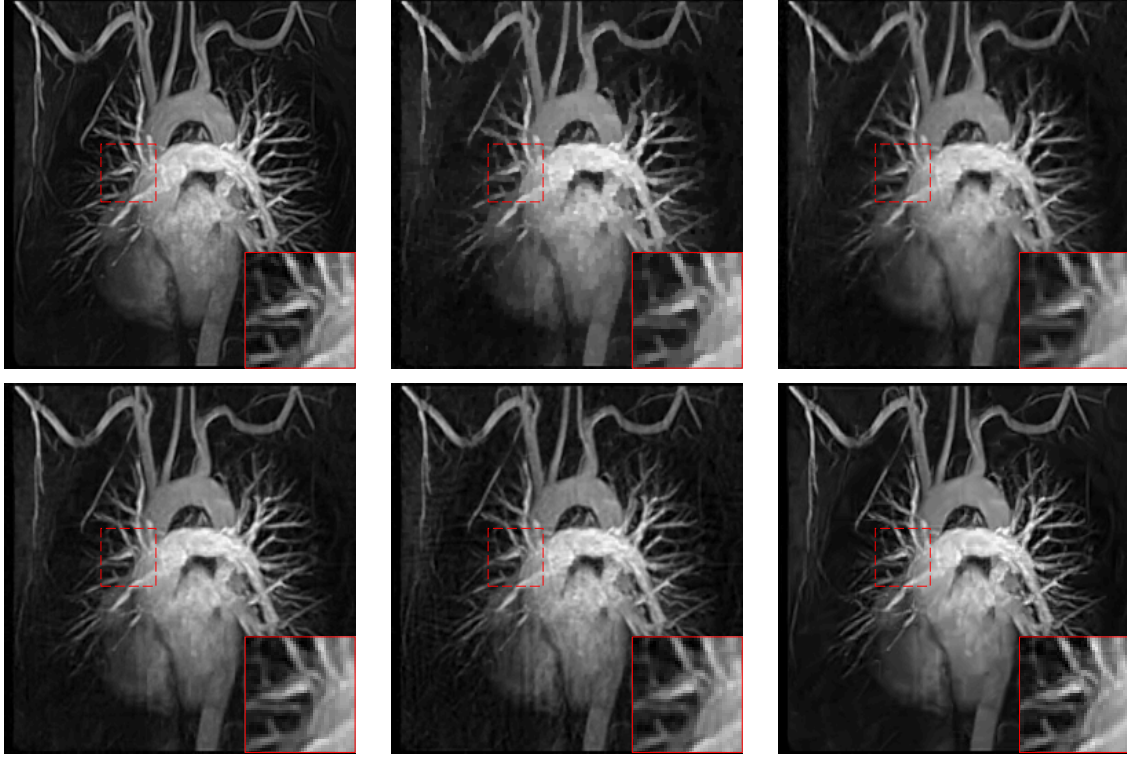


**Figure 5.** Magnitude of the real-valued chest image under 20% radial sampling. First row: Original (left), TV (middle), SIDWT (right). Second row: PANO (left), BM3D-IT (middle), BM3D-DAMP (right).

Now, we will use the equality  $\mathcal{F}\mathcal{F}_\Omega^H\mathcal{F}_\Omega\mathcal{F}^H = \mathbf{\Lambda}_\Omega$ , where  $\mathbf{\Lambda}_\Omega$  is a diagonal matrix equal to one at the diagonal elements  $k \in \Omega$  and zero everywhere else.

$$\begin{aligned}
 \mathcal{F}\hat{\mathbf{x}} &= \mathcal{F}\mathbf{x}_0 + (\mathbf{\Lambda}_\Omega + \alpha\mathbf{I}_N)^{-1}\mathbf{\Lambda}_\Omega\mathcal{F}(\mathbf{x}_{\text{ZF}} - \mathbf{x}_0) \\
 &= \mathcal{F}\mathbf{x}_0 + \frac{1}{1+\alpha}\mathbf{\Lambda}_\Omega\mathcal{F}(\mathbf{x}_{\text{ZF}} - \mathbf{x}_0) \\
 &= \mathcal{F}\mathbf{x}_0 + \frac{1}{1+\alpha}\mathcal{F}\mathcal{F}_\Omega^H\mathcal{F}_\Omega\mathcal{F}^H\mathcal{F}(\mathbf{x}_{\text{ZF}} - \mathbf{x}_0) \\
 (20) \quad &= \mathcal{F}\mathbf{x}_0 + \frac{1}{1+\alpha}\mathcal{F}\mathcal{F}_\Omega^H\mathcal{F}_\Omega(\mathbf{x}_{\text{ZF}} - \mathbf{x}_0) \\
 &= \mathcal{F}\mathbf{x}_0 + \frac{1}{1+\alpha}\mathcal{F}\mathcal{F}_\Omega^H(\mathbf{y} - \mathcal{F}_\Omega\mathbf{x}_0).
 \end{aligned}$$

We take the inverse Fourier transform of both sides to obtain the desired result:

$$(21) \quad \hat{\mathbf{x}} = \mathbf{x}_0 + \frac{1}{1+\alpha}\mathcal{F}_\Omega^H(\mathbf{y} - \mathcal{F}_\Omega\mathbf{x}_0).$$

**Acknowledgment.** We thank the anonymous reviewers for their insightful comments.

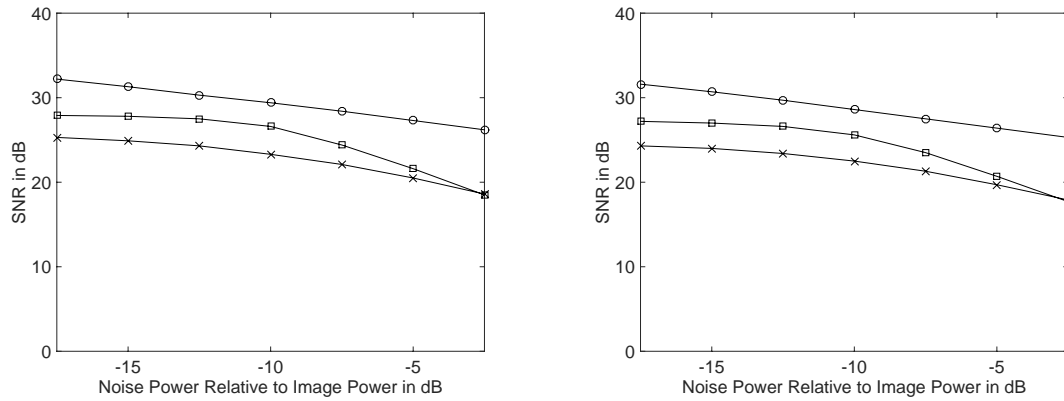


**Figure 6.** Reconstruction SNR for ZF (cross), PANO (square), and BM3D-DAMP (circle) algorithms under 20% radial sampling and various noise levels. Left: brain1 MR image. Right: brain2 MR image.

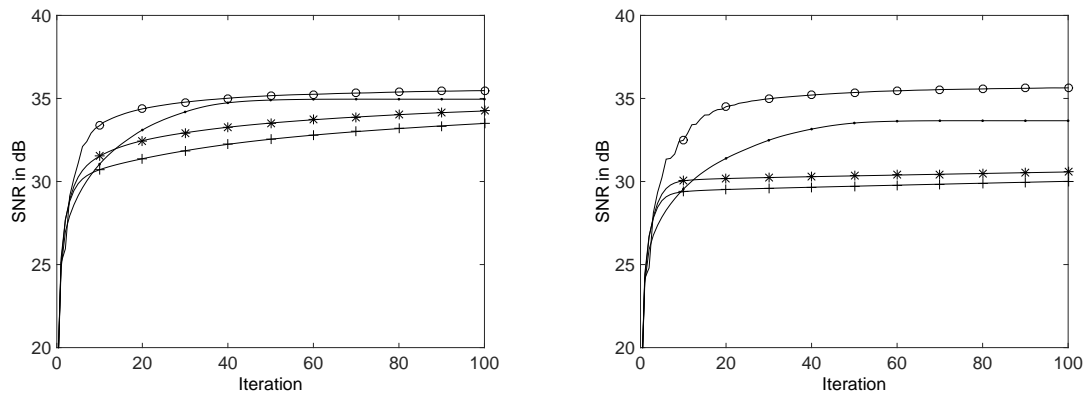


**Figure 7.** Convergence of HOSVD based BM3D-IT (point), IC based BM3D-IT (plus), BM3D-IT (star), and BM3D-DAMP (circle) algorithms under 20% radial sampling. Left: brain1 MR image. Right: brain2 MR image.

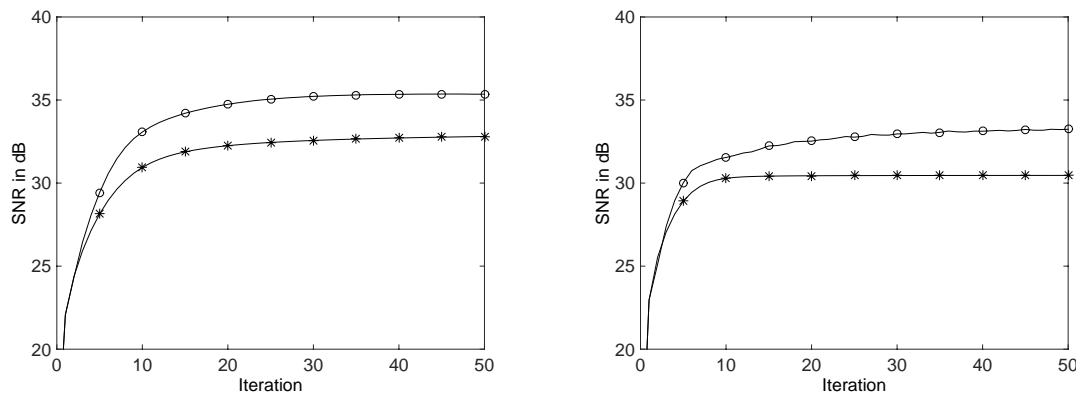


**Figure 8.** Convergence of BM3D-IT (star) and BM3D-DAMP (circle) algorithms under 20% radial sampling. Left: bust MR image. Right: chest MR image.

## REFERENCES

- [1] S. H. CHAN, X. WANG, AND O. A. ELGENDY, *Plug-and-play ADMM for image restoration: Fixed-point convergence and applications*, IEEE Trans. Comput. Imaging, 3 (2017), pp. 84–98, <https://doi.org/10.1109/TCL.2016.2629286>.
- [2] P. CHATTERJEE AND P. MILANFAR, *Is denoising dead?*, IEEE Trans. Image Process., 19 (2010), pp. 895–911, <https://doi.org/10.1109/TIP.2009.2037087>.
- [3] C. CHEN AND J. HUANG, *Exploiting the wavelet structure in compressed sensing MRI*, Magnetic Resonance Imaging, 32 (2014), pp. 1377–1389, <https://doi.org/10.1016/j.mri.2014.07.016>.
- [4] S. CHEN, C. LUO, B. DENG, Y. QIN, H. WANG, AND Z. ZHUANG, *BM3D vector approximate message passing for radar coded-aperture imaging*, in 2017 Progress in Electromagnetics Research Symposium - Fall (PIERS - FALL) (Singapore), IEEE, Washington, DC, 2017, pp. 2035–2038, <https://doi.org/10.1109/PIERS-FALL.2017.8293472>.
- [5] K. DABOV, A. FOI, V. KATKOVNIK, AND K. EGIAZARIAN, *Image denoising by sparse 3-D transform-domain collaborative filtering*, IEEE Trans. Image Process., 16 (2007), pp. 2080–2095, <https://doi.org/10.1109/TIP.2007.901238>.
- [6] A. DANIELYAN, V. KATKOVNIK, AND K. EGIAZARIAN, *BM3D frames and variational image deblurring*, IEEE Trans. Image Process., 21 (2012), pp. 1715–1728, <https://doi.org/10.1109/TIP.2011.2176954>.
- [7] I. DAUBECHIES, M. DEFRISE, AND C. DE MOL, *An iterative thresholding algorithm for linear inverse problems with a sparsity constraint*, Comm. Pure Appl. Math., 57 (2004), pp. 1413–1457, <https://doi.org/10.1002/cpa.20042>.
- [8] D. L. DONOHO, A. MALEKI, AND A. MONTANARI, *Message-passing algorithms for compressed sensing*, Proc. Natl. Acad. Sci. USA, 106 (2009), pp. 18914–18919, <https://doi.org/10.1073/PNAS.0909892106>.
- [9] M. J. EHRHARDT AND M. M. BETCKE, *Multicontrast MRI reconstruction with structure-guided total variation*, SIAM J. Imaging Sci., 9 (2016), pp. 1084–1106, <https://doi.org/10.1137/15M1047325>.
- [10] E. M. EKSGLOU, *Decoupled algorithm for MRI reconstruction using nonlocal block matching model: BM3D-MRI*, J. Math. Imaging Vis., 56 (2016), pp. 430–440, <https://doi.org/10.1007/s10851-016-0647-7>.
- [11] M. ELAD, *Why simple shrinkage is still relevant for redundant representations?*, IEEE Trans. Inform. Theory, 52 (2006), pp. 5559–5569, <https://doi.org/10.1109/TIT.2006.885522>.
- [12] M. ELAD, *Sparse and Redundant Representations: From Theory to Applications in Signal and Image Processing*, Springer, New York, 2010.
- [13] B. K. GUNTURK AND X. LI, *Image Restoration: Fundamentals and Advances*, CRC Press, Boca Raton, FL, 2012.
- [14] A. P. HARRISON, Z. XU, A. POURMORTEZA, D. A. BLUEMKE, AND D. J. MOLLURA, *A multichannel block-matching denoising algorithm for spectral photon-counting CT images*, Med. Phys., 44 (2017), pp. 2447–2452, <https://doi.org/10.1002/mp.12225>.
- [15] O. S. JAHROMI, B. A. FRANCIS, AND R. H. KWONG, *Relative information of multi-rate sensors*, Inform. Fusion, 5 (2004), pp. 119–129, <https://doi.org/10.1016/J.INFFUS.2004.01.003>.
- [16] J. HUANG, S. ZHANG, AND D. METAXAS, *Efficient MR image reconstruction for compressed MR imaging*, Med. Image Anal., 15 (2011), pp. 670–679, <https://doi.org/10.1016/j.media.2011.06.001>.
- [17] V. KATKOVNIK AND K. EGIAZARIAN, *Sparse phase imaging based on complex domain nonlocal BM3D techniques*, Digital Signal Process., 63 (2017), pp. 72–85, <https://doi.org/10.1016/j.dsp.2017.01.002>.
- [18] V. KATKOVNIK, M. PONOMARENKO, AND K. EGIAZARIAN, *Sparse approximations in complex domain based on BM3D modeling*, Signal Process., 141 (2017), pp. 96–108, <https://doi.org/10.1016/j.sigpro.2017.05.032>.
- [19] F. LI AND T. ZENG, *A universal variational framework for sparsity-based image inpainting*, IEEE Trans. Image Process., 23 (2014), pp. 4242–4254, <https://doi.org/10.1109/TIP.2014.2346030>.
- [20] F. LI AND T. ZENG, *A new algorithm framework for image inpainting in transform domain*, SIAM J. Imaging Sci., 9 (2016), pp. 24–51, <https://doi.org/10.1137/15M1015169>.
- [21] L. LIU, Z. XIE, AND C. YANG, *A novel iterative thresholding algorithm based on plug-and-play priors for compressive sampling*, Future Internet, 9 (2017), 24, <https://doi.org/10.3390/FI9030024>.

- [22] S. LIU, J. CAO, H. LIU, X. SHEN, K. ZHANG, AND P. WANG, *MRI reconstruction using a joint constraint in patch-based total variational framework*, J. Vis. Commun. Image Represent., 46 (2017), pp. 150–164, <https://doi.org/10.1016/j.jvcir.2017.03.017>.
- [23] M. LUSTIG, D. DONOHO, AND J. PAULY, *Sparse MRI: The application of compressed sensing for rapid MR imaging*, Magnetic Resonance Med., 58 (2007), pp. 1182–1195, <https://doi.org/10.1002/MRM.21391>.
- [24] J. MA AND L. PING, *Orthogonal AMP*, IEEE Access, 5 (2017), pp. 2020–2033, <https://doi.org/10.1109/ACCESS.2017.2653119>.
- [25] A. MALEKI, *Approximate Message Passing Algorithms for Compressed Sensing*, Ph.D. thesis, Stanford University, Stanford, CA, 2011.
- [26] C. A. METZLER, A. MALEKI, AND R. G. BARANIUK, *BM3D-PRGAMP: Compressive phase retrieval based on BM3D denoising*, in Proceedings of the IEEE International Conference on Image Processing (ICIP), IEEE, Washington, DC, 2016, pp. 2504–2508, <https://doi.org/10.1109/ICIP.2016.7532810>.
- [27] C. A. METZLER, A. MALEKI, AND R. G. BARANIUK, *From denoising to compressed sensing*, IEEE Trans. Inform. Theory, 62 (2016), pp. 5117–5144, <https://doi.org/10.1109/TIT.2016.2556683>.
- [28] A. PERELLI AND M. E. DAVIES, *Compressive computed tomography image reconstruction with denoising message passing algorithms*, in Proceedings of the 23rd European Signal Processing Conference (EUSIPCO), IEEE, Washington, DC, 2015, pp. 2806–2810, <https://doi.org/10.1109/EUSIPCO.2015.7362896>.
- [29] J. G. PROAKIS AND D. K. MANOLAKIS, *Digital Signal Processing: Principles, Algorithms and Applications*, Pearson, Upper Saddle River, NJ, 2006.
- [30] X. QU, Y. HOU, F. LAM, D. GUO, J. ZHONG, AND Z. CHEN, *Magnetic resonance image reconstruction from undersampled measurements using a patch-based nonlocal operator*, Med. Image Anal., 18 (2014), pp. 843–856, <https://doi.org/10.1016/J.MEDIA.2013.09.007>.
- [31] S. RAMANI, T. BLU, AND M. UNSER, *Monte-Carlo SURE: A black-box optimization of regularization parameters for general denoising algorithms*, IEEE Trans. Image Process., 17 (2008), pp. 1540–1554, <https://doi.org/10.1109/TIP.2008.2001404>.
- [32] S. RAMANI, X. WANG, L. FU, AND M. LEXA, *Denoising-based accelerated statistical iterative reconstruction for X-ray CT*, in Proceedings of the 4th International Conference on Image Formation in X-Ray Computed Tomography, Bamberg, Germany, 2016, pp. 395–398.
- [33] S. RANGAN, P. SCHNITER, AND A. FLETCHER, *On the convergence of approximate message passing with arbitrary matrices*, in Proceedings of the IEEE International Symposium on Information Theory, IEEE, Washington, DC, 2014, pp. 236–240, <https://doi.org/10.1109/ISIT.2014.6874830>.
- [34] S. RANGAN, P. SCHNITER, AND A. K. FLETCHER, *Vector approximate message passing*, in Proceedings of the IEEE International Symposium on Information Theory (ISIT), IEEE, Washington, DC, 2017, pp. 1588–1592, <https://doi.org/10.1109/ISIT.2017.8006797>.
- [35] S. RANGAN, P. SCHNITER, E. RIEGLER, A. K. FLETCHER, AND V. CEVHER, *Fixed points of generalized approximate message passing with arbitrary matrices*, IEEE Trans. Inform. Theory, 62 (2016), pp. 7464–7474, <https://doi.org/10.1109/TIT.2016.2619365>.
- [36] M. RIZKINIA, T. BABA, K. SHIRAI, AND M. OKUDA, *Local spectral component decomposition for multi-channel image denoising*, IEEE Trans. Image Process., 25 (2016), pp. 3208–3218, <https://doi.org/10.1109/TIP.2016.2561320>.
- [37] Y. ROMANO, M. ELAD, AND P. MILANFAR, *The little engine that could: Regularization by denoising (RED)*, SIAM J. Imaging Sci., 10 (2017), pp. 1804–1844, <https://doi.org/10.1137/16M1102884>.
- [38] S. SREEHARI, S. V. VENKATAKRISHNAN, B. WOHLBERG, G. T. BUZZARD, L. F. DRUMMY, J. P. SIMMONS, AND C. A. BOUMAN, *Plug-and-play priors for bright field electron tomography and sparse interpolation*, IEEE Trans. Comput. Imaging, 2 (2016), pp. 408–423, <https://doi.org/10.1109/TCL.2016.2599778>.
- [39] H. TALEBI AND P. MILANFAR, *Asymptotic performance of global denoising*, SIAM J. Imaging Sci., 9 (2016), pp. 665–683, <https://doi.org/10.1137/15M1020708>.
- [40] J. TAN, Y. MA, AND D. BARON, *Compressive imaging via approximate message passing with image denoising*, IEEE Trans. Signal Process., 63 (2015), pp. 2085–2092, <https://doi.org/10.1109/TSP.2015.2408558>.

- [41] S. V. VENKATAKRISHNAN, L. F. DRUMMY, M. JACKSON, M. D. GRAEF, J. SIMMONS, AND C. A. BOUMAN, *Model-based iterative reconstruction for bright-field electron tomography*, IEEE Trans. Comput. Imaging, 1 (2015), pp. 1–15, <https://doi.org/10.1109/TCI.2014.2371751>.
- [42] J. VILA, P. SCHNITER, S. RANGAN, F. KRZAKALA, AND L. ZDEBOROV, *Adaptive damping and mean removal for the generalized approximate message passing algorithm*, in Proceedings of the IEEE International Conference on Acoustics, Speech and Signal Processing (ICASSP), IEEE, Washington, DC, 2015, pp. 2021–2025, <https://doi.org/10.1109/ICASSP.2015.7178325>.
- [43] Y.-W. WEN, M. K. NG, AND W.-K. CHING, *Iterative algorithms based on decoupling of deblurring and denoising for image restoration*, SIAM J. Sci. Comput., 30 (2008), pp. 2655–2674, <https://doi.org/10.1137/070683374>.
- [44] M. ZIBULEVSKY AND M. ELAD, *L1-L2 optimization in signal and image processing*, IEEE Signal Process. Mag., 27 (2010), pp. 76–88, <https://doi.org/10.1109/MSP.2010.936023>.